Investigating the mechanical and optical properties of thin PDMS film by flat-punched indentation

Jae Sung Park[1], Rachel Cabosky[2], Zhijiang Ye[2], and Iltai (Isaac) Kim[1,*]

[1] Department of Engineering, Texas A&M University – Corpus Christi, TX, 78412-5797

[2] Department of Mechanical and Manufacturing Eng., Miami University, Oxford, OH, 45056

[*] Email: ikim@tamucc.edu

Abstract

We investigated mechanical and optical properties of a thin polydimethylsiloxane (PDMS) film through a flat-punched indentation experiment and a finite element simulation. A microscopic imaging method was used to measure the compressive strain of thin PDMS films, and its corresponding bulk refractive index (RI) was estimated using the relation between density and refractive index. A total internal reflection (TIR) experiment was conducted to estimate the local RI values near the bottom surface of PDMS film. We obtained the correlations between force and indentation displacement in thin PDMS films (10~70 micron). Stress-strain curves present the non-linear deformation of PDMS film with the instantaneous modulus depending on the load and the thickness. Poisson's ratio of PDMS film is estimated by fitting with Yang's asymptotic solution and is inversely proportional to the aspect ratio between the radius of the flat punch probe and the film thickness. RI of PDMS film increases with the decreasing film thickness as well as the increasing load. The bulk RI was increased up to 1.476 by the compressing load while the bottom-surface RI was increased only up to 1.435. This difference is explained qualitatively through the localized stress-strain distribution from finite element analysis. An inhomogeneous stress-strain distribution is observed in the simulation with lower strain at the bottom of the film, corresponding to experiment. A lower strain leads to lower local density resulting in a lower refractive index. Our research provides fundamental insights into the correlation between mechanical and optical properties of thin polymer films.

Keywords: Flat-punched indentation, PDMS thin film, Stress-strain, Total internal reflection, Microscopic imaging, Refractive index, Finite element analysis.

1. Introduction

Understanding the stress distribution in a microstructure is very significant for the development of microelectromechanical system (MEMS) devices such as flexible displays, Li-ion battery, tunable optics, or micro actuators [1-4]. Recently, MEMS devices are becoming smaller, thinner, and more complex with multi-layer structure or a shortened gap between elements to achieve high performance within the limited volume. This compact design can cause the malfunction in operation, provided a mechanical stress is exerted on the system. The mechanical stress can come from external causes, e.g., the bending of flexible organic light-emitting diode (OLED) display [5] or the swelling due to the heat generation of Li-ion battery [6-8]. In more severe cases, the constraint stress can result in a crack at the substrate layer of system [9, 10]. From these reasons, it is necessary to investigate the internal stress distribution of microscale thin film structure for the development of high performance MEMS device.

The mechanical stress induces the deformation of physical dimension of film layer and it thus can affect the internal density field of the film [11]. In general, the density change of material results in the alteration of refractive index, which can be elucidated by using molar refractivity such as Lorentz-Lorenz equation [12-14]. Based on this correlation, the internal mechanical properties can be estimated by experimentally measuring optical properties. Researchers tried to develop optical method to measure mechanical stress distributed in material [15, 16], and someone studied about the influence of mechanical stress on optical properties of materials [17-19]. A large number of studies about the stress-induced optical properties have been devoted mostly to macro-sized samples [11, 20, 21] and by a simulation approach [22, 23]. In addition, most of the mechanical stresses in the previous studies are with tension force [24-26]. Only a few works introduced optical and mechanical properties for micro-scale specimen [27]. It is very rare to find experimental studies for microscale specimen subjected to compressive stress. In this paper, we investigate the difference between bulk and near-surface values in the optical, physical properties of micro thin film subjected to compressive indentation load by using optical manners.

We apply two optical measurements to estimate bulk and local values of refractive index of thin film. First, the near-field optical method based on total internal reflection (TIR) is employed to measure critical TIR angles, which are related with the local refractive index around the bottom

surface of thin film. Second, the far-field imaging with a regular bright field microscope is employed to measure the film's bulk deformation, and then the bulk refractive index is estimated using molar refractivity. Through the comparison between bulk and local values of refractive indices, we estimate the variation of density field inside film subjected to compressive stress. To verify experimental data, we conduct finite element simulations showing the distributions of internal stress and density in thin film.

2. Theoretical Background

2.1 Flat punch indentation

The flat punch indentation of a compressible elastic film bonded to a rigid substrate was previously studied using asymptotic analysis by Yang [28]. When the contact radius (a) of the indenter is much larger than the film thickness (h), the indentation load (F) is proportional to the indentation depth (δ), contact area (A), and elastic properties of film while it is inversely proportional to the film thickness as follows:

$$F = \frac{\pi\delta a^2(\lambda+2G)}{h} = \frac{(1-\nu)\delta AE}{(1+\nu)(1-2\nu)h}\,. \tag{1}$$

Young's modulus (E) of sample is determined with Poisson's ratio (ν) and effective modulus (E_{eff}) which as follows:

$$E = [1-\nu^2]E_{\text{eff}}\,. \tag{2}$$

This simple relation is employed to indentation modeling when the Young's modulus of the rigid substrate is much greater than that of sample. For the indentation involving large deformation, the effective modulus is defined with the stiffness (S) and the non-linear factor (κ) of sample [29] as follows:

$$E_{\text{eff}} = \mathrm{S}/2a\kappa. \tag{3}$$

Instantaneous stiffness is defined as the derivative of force with respect to displacement (S = dF/dδ). The value of κ is estimated using the formula introduced in Zhang et. al.'s paper [30].

2.2 Relation between density and refractive index

The relation between the refractive index and the mass density of a substance was developed from the correlation of two polarization equations induced with molecular polarizability and dielectric constant as follows [12, 13]:

$$\frac{(n^2-1)}{4\pi + b(n^2-1)} = \frac{N_A \cdot \alpha}{M}\rho, \tag{4}$$

where n is refractive index, N_A is the universal Avogadro's number, α is volume molecular polarizability, ρ is density, and M is the molecular weight of the given material. By setting b = 4π/3, the most often used formula, Lorentz-Lorenz (L-L) relation is given [12, 13] as follows:

$$\frac{n^2-1}{n^2+2} = \frac{4\pi}{3}\frac{N_A \alpha}{M}\rho. \tag{5}$$

Based on the assumption that the polarizability of material is independent of its density, the fractional term of '$4\pi N_A \alpha/3M$' can be replaced by a constant 'k', and the L-L relation is simplified as:

$$\frac{(n^2-1)}{(n^2+2)}\frac{1}{\rho} = k. \tag{6}$$

From the above simple relation, we presume that the refractive index is a function of density as follows:

$$n = \sqrt{\frac{2k\rho+1}{1-k\rho}}, \tag{7}$$

where the constant k is obtained from Eq. (6) with the referred values for the refractive index and density at the unloaded, normal condition. From the above equation (7), the final value of refractive index after compression can be determined with the final density of material that is estimated using strain data. More details will be described in the result section 4.4.

Dislike the direct estimation of final density using Eq. (7), the refractive index change can be applied to determine the final value of refractive index. By differentiating the refractive index n in Eq. (4) with respect to density ρ, the relation between refractive index change (Δn) and density change ($\Delta\rho$) can be expressed as follows:

$$\frac{\Delta n}{\Delta \rho} \approx \frac{dn}{d\rho} = \frac{(n^2-1)\cdot(4\pi+bn^2-b)}{8\pi n\rho}, \tag{8}$$

where this differentiation is based on the assumption that the polarizability in Eq. (4) is independent of density. The density change rate ($\Delta\rho/\rho$) of the sample can be obtained in terms of the original and final volumes as follows:

$$\frac{\Delta\rho}{\rho_o} = \frac{\rho_f}{\rho_o} - 1 = \frac{V_o}{V_f} - 1, \quad (9)$$

where ρ_o and V_o are the original density and volume of the sample before compression, and ρ_f and V_f are the final density and volume at the end of compression, respectively. Then the refractive index change is calculated by the following equations:

$$\Delta n = \frac{(n^2-1)\cdot(4\pi+bn^2-b)}{8\pi n}\left(\frac{\rho_f}{\rho_o} - 1\right), \quad (10)$$

$$\Delta n = \frac{(n^2-1)\cdot(4\pi+bn^2-b)}{8\pi n}\left(\frac{V_o}{V_f} - 1\right), \quad (11)$$

where n is the original refractive index of the given material before compression. The index change Δn is dependent on the value of constant 'b', e.g. b = 0 according to Drude formula, b = 0.5 according to the empirical data of Ritland [12], b = 2.1 according to Gladstone-Dale (G-D) formula, and $b = 4\pi/3$ according to Lorentz-Lorenz (L-L) formula.

3. Experimental

3.1 Chemical, mechanical properties of PDMS material

We used a commercial PDMS elastomer named *Sylgard* 184 (Dow Corning) which consists of two components, a base (Part A) and a curing agent (Part B). The base contains poly-dimethylsiloxane ($-[OSi(CH_3)_2]_x-$) polymer having a silicon vinyl group ($SiCH=CH_2$), and the curing agent contains a different PDMS polymer having silicon hydride groups (SiH). Through the mixing of both components, two functional groups are bonded by hydrosilation reaction that is catalyzed by platinum and form $Si-CH_2-CH_2-Si$ linkage [31]. The multiple reaction allows three-dimensional cross-linking structure. The typical chemical formula of base is $CH_2=(CH)(CH_3)_2Si-[OSi(CH_3)_2]_x-OSi(CH_3)_2(CH)=CH_2$ with the average number of x = 60 [32]. The curing agent has a chemical formula $(CH_3)_3Si-[OSiH(CH_3)]_m-[OSi(CH_3)_2]_n-OSi(CH_3)_3$, where m = 3 and n = 7 in average [32].

The value of b in the Eq. (4) can be specified by estimating a molecular weight M and a molecular polarizability α. The molecular weight M is approximately {348.82 + 74.16(x+n) + 60.13m} g/mol based on the chemical formulas of base and curing agent. With x = 60, m = 3 and n = 7, M of the PDMS cross-linking is estimated as 5,498 g/mol. The molecular polarizability α is obtained from the sum of polarizabilities of all atoms composing of the cross-linked compound.

The polarizability of each atom is α_H = 0.484×10^{-40} F·m^2, α_C= 1.064×10^{-40} F·m^2, α_O= 0.671×10^{-40} F·m^2, and α_{Si}= 4.17×10^{-40} F·m^2 [33]. Based on the number of atoms in the cross-link (H-450, C-151, O-72, Si-74), the estimated molecular polarizability is approximately 7.354×10^{-38} F·m^2 that is equivalent to 6.609×10^{-22} cm^3 in the CGS system of units. With these estimations, $\frac{N_A}{M}\alpha$ is calculated to around 0.0724 cm^3/g. Then, by applying the refractive index of n = 1.4225 and an average density of ρ = 0.982 g/cm^3 for the cured *Sylgard* 184 PDMS [34, 35], the value of b is estimated as follows:

$$b = \frac{1}{\beta\rho} - \frac{4\pi}{n^2-1} = 1.788 \approx \frac{4\pi}{7}, \tag{12}$$

where β denotes $\frac{N_A}{M}\alpha$ in a unit of cm^3/g. The value of 1.788 is in between Drude (b=0) and Gladstone-Dale (b=2.1).

3.2 Fabrication of thin PDMS film

The two components in *Sylgard* 184 PDMS elastomer mixed with the composition ratio of 10:1 by weight using manual agitation for 10 minutes. The prepared PDMS mixture is usually full of bubbles, which are removed by the degassing process using a desiccator and a vacuum pump. Then, a spin-coater was used to produce PDMS films as thin as 10 to 100 μm. A slide glass (SF10, n = 1.732 at 633 nm) was placed on the spin-coater stage, and the 1 ml of PDMS mixture was poured on the slide. The initially designed thicknesses of PDMS films were 10, 25, 50, and 100 μm. However, the film thickness was influenced by experimental factors, i.e., spin speed, duration, density and viscosity of PDMS mixture, volume and initial thickness of PDMS pour on substrate. The spin speed was adjusted to 5850, 2340, 1170, and 585 RPM for 10, 25, 50, and 100-μm thicknesses, respectively with the consistent duration of 60 seconds. The viscosity of PDMS mixture is variable according to different mixing ratios between pre-polymer and curing agent. We employed the consistent mixing ratio of 10 to 1 in this experiment. After finishing the spin-coating process, PDMS film was cured with a hot plate at 90 °C for 1 hour. The accurate thicknesses of PDMS film were measured by using a microscope after the entire fabrication process is complete, which were 10, 20, 35 and 70 μm.

3.3 Microscopic imaging for the measurement of indentation displacement

We applied an optical microscopic imaging in order to measure indentation displacements depending on different film thicknesses and compressive loads (Fig. 1a) [36]. This imaging method utilizes a high-magnification lens configuration (objective lens: Mitutoyo 20X, WD 20 mm, and tube lens: 2X) and a high-resolution digital camera (PixeLINK PL-B625, 2592×1944 pixels), which can fulfill 80 nm precision in displacement measurement. A PDMS-coated slide glass was placed on a rigid metal plate as shown in Figure 1a. A small glass block (length × width × thickness = 2.4 × 3.4 × 1.0 mm^3) was employed as an indenter to exert the compressive force to the PDMS film. We applied the compressive stress up to 17 MPa with the maximum load of 14 kg on the indenter. The objective lens was focused on the sidewall of glass indenter and tracks the displacement of wall with increasing the compressive load. The tiny gap between metal plate and slide glass possibly involves uncertainty in the displacement measurement. Thus, we separately conducted a calibration test to measure the reference displacement by the bare slide glass without a PDMS film coating. The actual displacement of indentation was determined by subtracting the reference displacement from measurement data.

3.4 Total internal reflection (TIR) measurement

The local refractive index (RI) near the bottom surface of PDMS film was determined by utilizing a prism-based TIR refractometer system [37-39] (Fig. 1b). An equilateral triangle prism (SF10, n = 1.732 at 633 nm) is mounted on a translation stage which is combined with a vertical post, and a He-Ne laser (λ = 633 nm) is mounted on a straight rail which pivots around the prism. A digital protractor (resolution = 0.01°, accuracy = 0.05°) is attached to the rail. A PDMS-coated slide glass is placed on the upper surface of prism. A collimated beam (d = 0.8 mm) emitted from the light source is incident on the left surface of prism, and after passing through prism and slide glass it is then reflected on the interface between PDMS film and slide glass. The incident angle of beam reflected on the PDMS-glass interface is calculated from the rail angle measured by the protractor using Snell's law, i.e., $\sin(30° - \theta_{rail}) = n_{SF10} \sin(\theta_{incident} - 60°)$. The total-internal-reflected laser beam at the PDMS-glass interface comes out of the right side of prism, and its intensity is observed using a viewing screen while the incident angle decreases from 60° to 50°. There are two observation spots as depicted in Fig. 1b. One spot locating at the right-bottom side of prism is to monitor the TIR condition of incident beam, and the second spot around the right corner of prism is used to find the critical angle (θ_c) of TIR phenomenon. In the case of TIR, there is no beam

emanating from the PDMS-glass interface over the upper side of the prism, but beam coming out of the right-bottom side of the prism always exists, and only its intensity is changing. The critical angle is determined at the moment that the laser beam comes out of the right corner of prism as changing the incident angle. Finally, the local RI value near the bottom surface of PDMS film is estimated with the critical angle and Snell's law of $n_{\text{sample}} = n_{\text{prism}} \sin\theta_c$.

4. Results and discussions

Dependency of mechanical, optical properties by the flat punch indentation was investigated for thin PDMS film with the thicknesses of 10, 20, 35 and 70 μm. Each data point represents the average value obtained from 10 measurements, and all error bars indicate a 95% confidence interval.

4.1 Contact force vs. indentation displacement

The PDMS film deformed non-linearly when it was subjected to the compressive loading by a flat-punched indenter. The resultant correlation curves between applied force and indentation displacement are presented in terms of film thickness in Fig. 2. Each instantaneous displacement was obtained by comparing two consecutive images of the tested sample using the microscopic observation as described in the section 3.3. The absolute magnitude of displacement ranged in an order of micrometer that was dependent on the film thickness. The thinner the film thickness the smaller the displacement. However, the portion of displacement relative to film thickness increased much significantly at the thinner film rather than at the thicker one. This can be quantitatively explained with strain calculation that will be presented in the following section.

The patterns of all force-displacement curves are totally unlike a linear profile. All profiles seem be non-linear below the compressive force of 80 N and linear above the force of 80 N, which show the typical force-displacement characteristic of PDMS material [20, 40]. The profile slope of the linear section increased gradually with the decreasing film thickness. The 10- and 20-μm films display a significantly non-linear profile that looks like a '*J*' letter. From the feature of profile slope, it is verified that the thinnest film has the highest level of stiffness according to the compressive loading.

4.2 Stress vs. Strain

The longitudinal strains (ε_{zz}) which was defined as a measure of compression relative to initial length were determined with the raw data of vertical displacement presented in Fig. 2. The compressive stress was also expressed as the external pressure that was estimated with a loading force divided by a contact area of indenter. Figure 3 presents stress-strain curves in terms of different film thicknesses. The higher strain indicates the larger proportional deformation from the initial dimension. It is an interesting feature that the thinnest film possesses the highest strain. It is expected that the strain could increase more with the thinner film.

Overall, all stress-strain curves show the characteristic of nonlinear deformation. The slopes of all stress-strain curves hardly maintain constant during the deformation but increase gradually with increasing stress. In particular, in the case of the thinnest (10 μm) film, the stress-strain profile is featured with a drastic change in its slope at the low stress region below 8 MPa. This highly curved profile represents the typical pattern of stress-strain curve for non-linear material involving large deformation. Through the literature survey, it was verified that our experimental data were relatively analogous to the previously reported results [20].

In the flat punch indentation, the elastic modulus for an infinite thickness layer is driven from the linear stress-strain curve involving infinitesimal deformation. However, the indentation for a thin film with large deformation (> 10% strain) should consider the instantaneous deformation of stress-stress curve to estimate the non-linear elastic modulus [29]. Therefore, the compressive modulus of thin film PDMS sample was calculated with the presented experimental data of force and displacement, which was based on the analytical solutions presented in Eqs. (2) and (3). The concept of effective modulus (E_{eff}) and non-linear factor (κ) is employed to this estimation. Figure 4 shows the estimated values of instantaneous compressive modulus in terms of the applied force and film thickness. The calculated modulus is generally proportional to the applied force but inversely proportional to film thickness. In the low contact force, it is approximately close to the nominal value (2 MPa) of elastic modulus of the cured PDMS sample [21]. Although there is a partial fluctuation in the tendency of increasing modulus along with the decreasing thickness, we could estimate that the largest modulus was obtained with the thinnest film and the maximum loading. The dependency of elastic modulus on the film thickness is coincident with the previous results [27, 40, 41]. Note that Poisson's ratios used in Eq. (2) were separately obtained prior to the calculation of modulus, which will be described in the following section.

4.3 Poisson's ratio

In order to estimate Poisson's ratio, it is necessary to know longitudinal and transversal strains. However, it was difficult to measure the transversal strain in the flat-punch indentation test. We applied the analytical solution of force vs. displacement for the flat-punch indentation to estimate Poisson's ratio, as described in the preceding section 2.1. Figure 5 presents various correlation curves between force and displacement of experimental data (triangle symbol) and analytical solutions (solid and dashed lines) that comes from Eq. (1) in the section 2.1. The analytical solution lines changed according to different Poisson's ratio, which is supposed to be constant during the compression. By comparing the data symbol and the various solution lines, we found the best-fitted solution lines for each film thickness, which brought us different Poisson' ratios depending on the film thickness. Based on our estimation, the Poisson's ratio of 70-μm, 35-μm, 20-μm, and 10-μm film has a value of around 0.49, 0.486, 0.48, and 0.465, respectively.

The thickness dependence of Poisson's ratio can be elucidated by taking account of the geometric dimensions of the compressed zone. In general, the nominal Poisson's ratio of the cured PDMS sample is 0.49 that is applicable to the bulk specimen having a large thickness comparable to a contact region. This bulk quantity of 0.49 is associated with the averaged value of local distribution of Poisson's ratio, which has very low local value of Poisson's ratio near the contacting interfaces [42, 43]. In our flat-punched indentation test, an indenter and a substrate glass adhered tightly to a PDMS film due to the characteristics of clean, flat, sticky surfaces of PDMS film. The compressive loading also helped the interfaces between PDMS and glasses keep maintaining the bonded condition. This strong bonding effect induced the reduction of Poisson's ratio in the compressed PDMS film. Moreover, the tested specimens had much smaller film thicknesses than the lateral dimension of contact area. The ratio between probe's radius (a = 1.4 mm) and film thickness (h) is ranging from 20 to 140. Note that the probe's radius is based on the hydraulic diameter of the rectangular contact area (2.4mm x 3.4mm). The estimated values of Poisson's ratio is inversely proportional to this aspect ratio, a/t (see Fig. 6). As the aspect ratio increases, the bonding effect by top and bottom interfaces became more predominant in determining the bulk value of Poisson's ratio. In a physical point of view, the high aspect ratio attenuates the influence of vertical compressive pressure on the transversal extension of thin film. As the film thickness

was getting thinner, the feature of deformation would be further similar to uniaxial vertical compression mode, which might have the potential for the higher degree of RI.

4.4 Bulk density and refractive index of PDMS film

The change of bulk mass density can be estimated analytically based on the volumetric deformation. In the indentation on thin film, the uniaxial compressive force exerted on the film involves geometrical deformation made with longitudinal contraction and transversal extension. If there is no change in the chemical structure due to the compression, the final density (ρ_f) of the sample is determined with both strains of longitudinal and transversal directions [11] as follows:

$$\rho_f = \frac{\rho_0}{(1+\varepsilon_{zz})(1+\varepsilon_{xx})^2}, \tag{13}$$

where ρ_0 is the original density of unloaded sample and ε_{zz} and ε_{xx} are longitudinal and transverse strains, respectively. In this study, the transversal strain was estimated approximately by using Poisson's ratio that was obtained by the analytical solution of force-displacement, described in the previous section.

Figure 7a presents the bulk values of mass density (right axis) of PDMS film in terms of applied stresses and film thickness. The bulk density significantly increased at the thinnest film. This does not mean that the thinner film was compressed much easily compared to the thicker one. On the contrary, the thinner film has higher stiffness than the thicker one as indicated in the force-displacement relation of Fig. 2. The high bulk density of thin film can be explained with the higher longitudinal strain and the lower Poisson's ratio. The combination of these parameters made the flat-punch indentation on a thin film become close to a uniaxial compression mode.

The bulk values of refractive index (RI) were obtained by applying the final density ρ_f in Eq. (13) to the RI relation of Eq. (7). In another manner, it could be estimated using the RI change (Δn) which was calculated by inserting the density ratio (ρ_f/ρ_o) obtained from Eq. (13) into the RI change equation of Eq. (10) as follows:

$$\Delta n = \frac{(n^2-1)\cdot(4\pi+bn^2-b)}{8\pi n}\left\{\frac{1}{(1+\varepsilon_{zz})(1+\varepsilon_{xx})^2}-1\right\}, \tag{14}$$

which can be estimated differently according to the value of constant '*b*'. Figure 8 shows various RI lines of the cured *Sylgard* 184 PDMS as a function of density, which was calculated with Eq. (14) and five different values for '*b*' according to the applied relations.

Figure 7a presents the bulk RIs (left axis) of PDMS film in terms of applied stresses and film thickness, which were based on the L-L relation with the constant $b = 4\pi/3$. The estimated values of bulk RI increased with increasing the applied stress. They significantly increased with decreasing film thickness under the same stress condition. Based on the L-L relation, the RI value of the 10-μm film could reach the level of glycerol ($n = 1.476$). Then, the estimation of RI can be adjusted by applying other refractivity relations (Drude rule, Gladstone-dale rule, and Ritland's data) that were specified for the species of material. In the compression mode, the refractive index of material has higher value by the L-L relation compared to the other relations (see Fig. 8). Particularly, if we apply our analytical relation with the constant $b = 1.788$, the RI change (Δn) are reduced by 15% compared to the estimated by L-L relation (see Fig. 8). In this case, the maximum bulk RI of the compressed PDMS film becomes around $n = 1.467$ for the thinnest (10 μm) specimen. The value of b is associated with the deformable ions that may increase a near-neighbor interaction field, so-called the overlap field [13]. In the material with an ideal point-dipole lattice, the overlap field is barely formed and the L-L relation is applicable. Meanwhile, the effect of overlap field can increase in the cured PDMS material, which is composed of silica-based polymorphs. Consequently, the small value of $b = 1.788$ is the product by the deformable ionic structure of PDMS material. Until now, there has been no experimental data to confirm precisely the most optimal refractivity relation for the cured PDMS film. It is necessary to conduct the direct measurement of RI of the compressed PDMS film in the future.

The RI value might be increased up to the glass level if the high longitudinal strain (> 50 %) would be obtained by applying bigger stress. Due to the characteristics of the compressed PDMS, the increasing RI value is opening up a new way of fabricating PDMS-based tunable optics [3].

4.5 Bottom-surface density and refractive index of PDMS film

We measured refractive index (RI) near the bottom surface of PDMS film using a TIR method. The TIR phenomenon is generally characterized with an evanescent wave that penetrates into a PDMS layer up to the order of the wavelength of light source (0.633 μm). This means that the critical angle of TIR just represents the optical property of the restricted region close to the bottom surface of PDMS film. In addition, a laser beam ($d = 0.8$ mm) was reflected on a small spot with an oval shape of 1.5 mm × 0.8 mm. Consequently, the measurement data presented in Fig. 7b indicate the local RI values for the thin region near the bottom surface, corresponding to the oval

area of around 1.0 mm^2 and the thickness of 1~3 μm. The corresponding bottom-surface density of each RI value is also denoted on the right axis of Fig. 7b, which is estimated analytically using the Lorentz-Lorenz relation in Eq. (6).

Figure 7b is the representative result selected among several individual measurement data. This graph presents that much lower RI values were obtained compared to the predicted bulk RI values with very high compressive stress employed. In the case of 10-μm film, the maximum bottom-surface RI was approximately 1.435 at the stress of 17 MPa, which shows 0.88 % increase from a baseline (n = 1.4225). Meanwhile, the maximum bulk RI of 10-μm film was estimated to be roughly 1.476 with 3.76% increase from n = 1.4225. Arithmetically, the increase margin of bulk RI was about 4 times larger than that of bottom-surface RI. This numerical comparison shows the extreme case in the difference of RI values between bulk and local cases. As the film becomes thicker, the difference between bulk and bottom-surface RIs decreases gradually but the bulk RI is still larger than the bottom-surface RI. The high bulk RI comes from the high value of mass density. This is consistent with the previous indentation studies where lower density was observed near interface region [44-46]. That is, much denser material exists inside the film while lighter material is located near the surface. We can predict that the distribution of mass density is not homogeneous through the vertical line of film. This prediction is equally adaptable to the distribution of internal stress.

4.6 Finite element analysis

A commercial finite element software, Abaquos 2017 was used to verify the stress-strain distribution in a thin PDMS film and characterize the stresses and strains at the contact interface between a glass probe and a PDMS film. The contact area is identical with the experimental condition (2.4 mm × 3.4 mm). The PDMS film applied in simulation has different thicknesses of 10, 20, 40, 60, 80, and 100 μm. The geometry and mesh of model are illustrated in Fig. 9. A uniform pressure was applied on the top surface of glass probe. The lateral position of top surface of glass probe was constrained and the position of bottom surface of PDMS thin film was fixed which is consistent with experimental conditions. Figure 9 shows the contour images regarding the internal stress and strain distributed in the probe and film. Contour is depicted on the bottom surface of PDMS film as well as the central, vertical section of the entire specimen.

We verified that the internal distributions of stress and strain are totally non-uniform through the entire region, as observed in the difference between the bulk density from microscopic imaging and the bottom-surface density from TIR measurement as shown in Fig. 7. As we see the inside of glass probe, the high stress converges to the bottom and center area. Meanwhile, the stress and strain in PDMS film are concentrated under the probe's boundary lines, not under the center position of probe. The minimum stress and strain are built near the center, bottom surface of PDMS film, where is the interest zone searched by our TIR experiment.

Figure 10 shows the stress-displacement (Fig. 10a) and stress-strain (Fig. 10b) curves of the film under different applied stresses obtained from the finite element analysis. The strain increases with applied stress and decrease with increasing thickness of the film at given applied stress. This trend is qualitatively consistent with our experiments presented in Fig. 2 and 3.

Furthermore, we simulated the strain profile along the depth at the center area of thin film, corresponding to the reflected region by laser beam. Figure 11 shows the representative profile of local longitudinal strain (■ symbol), which is made with the compression of 10 MPa applied to a 80-μm thick film. It was observed that the strain reduced to the minimum value at the bottom surface of PDMS film, which indicates less volume compression at the bottom surface compared with the inside. The average strain ($\varepsilon_{zz,\,\mathrm{average}} = 0.112$) is corresponding to our experimental result of stress-strain data shown in Fig. 3. In addition, the local refractive index can be estimated from the local strains using Eq. (14) with $b = 4\pi/3$. Figure 11 shows the representative profile of the non-uniform distribution of refractive index (Δ symbol) along the vertical position. The low local density due to low strain at the film bottom leads to lower local refractive index than the bulk RI value resulting from the averaged density.

5. **Conclusions**

In summary, we studied the stress and the deformation of PDMS thin film at different loads by experiments and simulations. Microscopic imaging and total internal reflection methods are employed for experiments and finite element analysis is used for simulation. The measured stress and deformation are correlated with the refractive index of the film through Lorentz-Lorentz equation. We investigated not only the difference between the bulk and the bottom-surface RI values of PDMS film but also the RI dependency on the film thickness and the stress. The refractive index increases as the compressive stress increases, and the film thickness becomes thinner. TIR

measurement was useful for finding out the point value of refractive index on the a few micrometer layer from the bottom surface of sample film. This research provides a valid first step toward fully understanding the three-dimensional stress-strain distribution and the correlation of the mechanical and optical properties of thin film. In the future work, a pointwise scanning using TIR system can be feasible for measuring the lateral distribution of strain if the diameter of laser beam is reduced down to micrometer scale. The computational works showed that the compressive stress could change the distributions of density as well as refractive index due to the inhomogeneous distribution of internal stress. This information will be helpful for the development of optical devices or the monitoring of thin-film systems under mechanical stresses such as flexible electronics

Acknowledgements

This study was supported by a research grant from CEKO, Co., LTD and a Texas Comprehensive Research Fund grant from the Texas A&M University-Corpus Christi Division of Research, Commercialization and Outreach. R.C. and Z.Y. would like to acknowledge financial support from U.S. National Science Foundation [grant number CMMI-1362565].

References

[1] V.L. Pushparaj, M.M. Shaijumon, A. Kumar, S. Murugesan, L. Ci, R. Vajtai, R.J. Linhardt, O. Nalamasu, P.M. Ajayan, Flexible energy storage devices based on nanocomposite paper, PNAS USA 104(34) (2007) 13574-13577.

[2] K.A. Cook-Chennault, N. Thambi, A.M. Sastry, Powering MEMS portable devices-a review of non-regenerative and regenerative power supply systems with special emphasis on piezoelectric energy harvesting systems, Smart Mater. Structures 17(4) (2008) 043001.

[3] G. Beadie, M.L. Sandrock, M.J. Wiggins, R.S. Lepkowicz, J.S. Shirk, M. Ponting, Y. Yang, T. Kazmierczak, A. Hiltner, E. Baer, Tunable polymer lens, Opt. Express 16(16) (2008) 11847.

[4] R.P. Xu, Y.Q. Li, J.X. Tang, Recent advances in flexible organic light-emitting diodes, J. Mater. Chem. C 4 (2016) 9116-9142.

[5] M. Aleksandrova, Specifics and challenges to flexible organic light-emitting devices, Adv. Mater. Sci. Eng. 2016 (2016) 4081697.

[6] J. Cannarella, C.B. Arnold, Stress evolution and capacity fade in constrained lithium-ion pouch cells, J. Power Sources 245 (2014) 745-751.

[7] K.Y. Oh, J.B. Siegel, L. Secondo, S.U. Kim, N.A. Samad, J. Qin, D. Anderson, K. Garikipati, A. Knobloch, B.I. Epureanu, C.W. Monroe, A. Stefanopoulou, Rate dependence of swelling in lithium-ion cells, J. Power Sources 267 (2014) 197-202.

[8] X. Cheng, M. Pecht, In situ stress measurement techniques on Li-ion battery electrodes: A review, Energies 10 (2017) 591.

[9] T.Y. Tsui, A.J. McKerrow, Constraint effects on thin film channel cracking behavior, J. Mater. Res. 20(9) (2005) 2266-2273.
[10] H. Chai, Channel cracking in inelastic film/substrate systems, Int. J. Solids Structures 48 (2011) 1092-1100.
[11] I. Turek, N. Tarjanyi, I. Martincek, D. Kacik, Effect of mechanical stress on optical properties of polydimethylsiloxane, Opt. Mater. 36 (2014) 965-970.
[12] H.N. Ritland, Relation between refractive index and density of a glass at constant temperature, J. Amer. Ceram. Soc. 38(2) (1955) 86-88.
[13] O.L. Anderson, E. Schreiber, The relation between refractive index and density of minerals related to the earth's mantle, J. Geophys. Res. 70 (1965) 1463-1471.
[14] K. Sangwal, W. Kucharczyk, Relationship between density and refractive index of inorganic solids, J. Phys. D: Appl. Phys. 20 (1987) 522-525.
[15] T. Jakob, G. Kleideiter, W. Knoll, Thin films and interfaces at high pressure, Int. J. Polym. Anal. Charact. 9 (2004) 153-175.
[16] A.A. Oraevsky, S.L. Jacques, F.K. Tittel, Measurement of tissue optical properties by time-resolved detection of laser-induced transient stress, Appl. Opt. 36(1) (1997) 402-415.
[17] G.W. Scherer, Stress-induced index profile distortion in optical waveguides, Appl. Opt. 19(12) (1980) 2000-2006.
[18] W. Rieger, T. Metzger, H. Angerer, R. Dimitrov, O.A. Ambacher, M. Stutzmann, Influence of substrate-induced biaxial compressive stress on the optical properties of thin GaN films, Appl. Phys. Lett. 68(7) (1996) 970-972.
[19] C.C. Lee, C.L. Tien, JC. Hsu, Internal stress and optical properties of Nb_2O_5 thin films deposited by ion-beam sputtering, Appl. Opt. 41(10) (2002) 2043-2047.
[20] I.D. Johnston, D.K. McCluskey, C.K.L. Tan, M.C. Tracey, Mechanical characterization of bulk Sylgard 184 for microfluidics and microengineering, J. Micromech. Microeng. 24 (2014) 035017.
[21] Z. Wang, A.A. Volinsky, N.D. Gallant, Crosslinking effect on polydimethylsiloxane elastic modulus measured by custom-built compression instrument, J. Appl. Polym. Sci. 131(22) (2014) 41050.
[22] L. Su, A.Y. Yi, Investigation of the effect of coefficient of thermal expansion on prediction of refractive index of thermally formed glass lenses using FEM simulation, J. Non-Cry. Sol. 357 (2011) 3006–3012.
[23] J. Zhou, J. Yu, L.J. Lee, L. Shen, A.Y. Yi, Stress relaxation and refractive index change of As_2S_3 in compression molding, Int. J. Appl. Glass. Sci. 8 (2017) 255–265.
[24] P.Y. Fonjallaz, F. Cochet, B. Leuenberger, H.G. Limberger, R.P. Salathé. Tension increase correlated to refractive-index change in fibers containing UV-written Bragg gratings, Opt. Lett. 20(11) (1995) 1346-8.
[25] C.S. Kim, Y. Han, B.H. Lee, W.T. Han, U.C. Paek, Y. Chung, Induction of the refractive index change in B-doped optical fibers through relaxation of the mechanical stress, Opt. Commun. 185(4) (2000) 337-42.
[26] A.P. Gerratt, I. Penskiy, S. Bergbreiter, In situ characterization of PDMS in SOI-MEMS, J. Micromech. Microeng. 23(4) (2013) 045003.
[27] W. Xu, N. Chahine, T. Sulchek, Extreme hardening of PDMS thin films due to high compressive strain and confined thickness, Langmuir 27 (2011) 8470-8477.
[28] F. Yang, Asymptotic solution to axisymmetric indentation of a compressible elastic thin film, Thin Solid Films 515 (2006) 2274-2283.

[29] R.M. Delaine-Smith, S. Burney, F.G. Balkwill, M.M. Knight, Experimental validation of a flat punch indentation methodology calibrated against unconfined compression tests for determination of soft tissue biomechanics, J. Mech. Behav. Biomed. Mater. 60 (2016) 401-415.
[30] M. Zhang, Y.P. Zheng, A.F.T. Mak, Estimating the effective Young's modulus of soft tissues from indentation tests-nonlinear finite element analysis of effects of friction and large deformation, Med. Eng. Phys. 19 (1997) 512-517.
[31] A. Lamberti, M. Di Donato, A. Chiappone, F. Giorgis, G. Canavese, Tunable electromechanical actuation in silicone dielectric film, Smart Mater. Struct. 23 (2014) 105001.
[32] U.J. Ana, G.W. Critchlow, K.M. Ford, N.R. Godfrey, D.B. Grandy, M.A. Spence, A preliminary investigation into the apparent adhesive effect of stearic acid on cured silicone elastomer, Int. J. Adhesion Adhesives 30 (2010) 781-788.
[33] G.G. Raju, Dielectrics in electric fields, second ed., CRC press, Boca Raton, 2017.
[34] Dow Corning, Product information sheet of Sylgard® 184 silicone elastomer, Form No. 11-3184B-01, 2014.
[35] A.S. Cruz Felix, A. Santiago-Alvarado, F. Iturbide-Jimenez, B. Licona-Moran, Physical-chemical properties of PDMS samples used in tunable lenses, Int. J. Eng. Sci. Innovative Technol. 3 (2014) 563-571.
[36] L. Edelsten, J.E. Jeffrey, L.V. Burgin, R.M. Aspden, Viscoelastic deformation of articular cartilage during impact loading, Soft Matter 6 (2010) 5206-5212.
[37] G. Kleideiter, M.D. Lechner, W. Knoll, Pressure dependence of thickness and refractive index of thin PMMA-films investigated by surface plasmon and optical waveguide spectroscopy, Macromol. Chem. Phys. 200 (1999) 1028-1033.
[38] I. Kim, K. D. Kihm, Measuring near-field nanoparticle concentration profiles by correlating surface plasmon resonance reflectance with effective refractive index of nanofluids, Opt. Lett. 35(3) (2010) 393-395.
[39] S. Cheon, K.D. Kihm, H. Kim, G. Lim, J.S. Park, J.S. Lee, How to reliably determine the complex refractive index (RI) of graphene by using two independent measurement constraints, Scientific Reports 4 (2014) 6364.
[40] Y. Hang, G. Liu, K. Huang, W Jin, Mechanical properties and interfacial adhesion of composite membranes probed by in-situ nano-indentation/scratch technique, J. Membr. Sci. 494 (2015) 205-215.
[41] A. Selby, C. Maldonado-Codina, B. Derby, Influence of specimen thickness on the nanoindentation of hydrogels: Measuring the mechanical properties of soft contact lenses, J. Mech. Behav. Biomed. Mater. 35 (2014) 144-156.
[42] R.H. Pritchard, P. Lava, D. Debruyne, E.M. Terentjev, Precise determination of the Poisson ratio in soft materials with 2D digital image correlation, Soft Matter 9 (2013) 6037-6045.
[43] M. Angelidi, A.P. Vassilopoulos, T. Keller, Displacement rate and structural effects on Poisson ratio of a ductile structural adhesive in tension and compression, Int. J. Adhesion Adhesives 78 (2017) 13-22.
[44] Y.C. Lu, S.N.V.R.K. Kurapati, F. Yang, Finite element analysis of cylindrical indentation for determining plastic properties of materials in small volumes, J. Phys. D: Appl. Phys. 41 (2008) 115415.

[45] Z. Hu, K.J. Lynne, S.P. Markondapatnaikuni, F. Delfanian, Material elastic-plastic property characterization by nanoindentation testing coupled with computer modeling, Mater. Sci. Eng. A 587 (2013) 268-282.
[46] T.G. Murthy, C. Saldana, M. Hudspeth, R. M'Saoubi, Deformation field heterogeneity in punch indentation, Proc. Royal Soc. A 470 (2014) 20130807.

The list of figure captions

Figure 1. Schematic diagrams of experimental setups: (a) strain measurement and (b) TIR measurement.

Figure 2. Force-displacement curves about four different thicknesses of the cured PDMS film according to mechanical, compressive loading.

Figure 3. Stress-strain curves about four different thicknesses of the cured PDMS film according to mechanical, compressive loading.

Figure 4. Instantaneous Young's modulus of the cured PDMS film in terms of (a) compressive force and (b) film thickness, which is based on the theoretical correlations in Eq. (2) and (3).

Figure 5. Force-displacement curves based on theoretical analysis for the flat punch indentation on the cured PDMS film with different thicknesses of (a) 70 μm, (b) 35 μm, (c) 20 μm, and (d) 10 μm.

Figure 6. Poisson's ratio of the cured PDMS film as a function of the aspect ratio of probe radius to film thickness.

Figure 7. Refractive index (left axis) and density (right axis) of the cured PDMS film in terms of different compressive stress. (a) Bulk values of RI estimated using bulk strain data and theoretical calculation. (b) Bottom-surface values of RI obtained from TIR measurement.

Figure 8. Refractive index of the cured *Sylgard* 184 PDMS as a function of density according to different constant '*b*'.

Figure 9. Cross-section views of (a) stress and (b) strain contour maps made with finite element model of a glass probe compressing on a PDMS film at the thickness of 80 μm and the applied stress of 5 MPa.

Figure 10. (a) Stress-displacement curves and (b) stress-strain curves in terms of different film thickness and applied stress.

Figure 11. The depth-wise local strain (■) and refractive index (Δ) in the restricted area at the center of PDMS film (80 μm), which is designated as the reflected zone of laser beam in TIR circumstance.

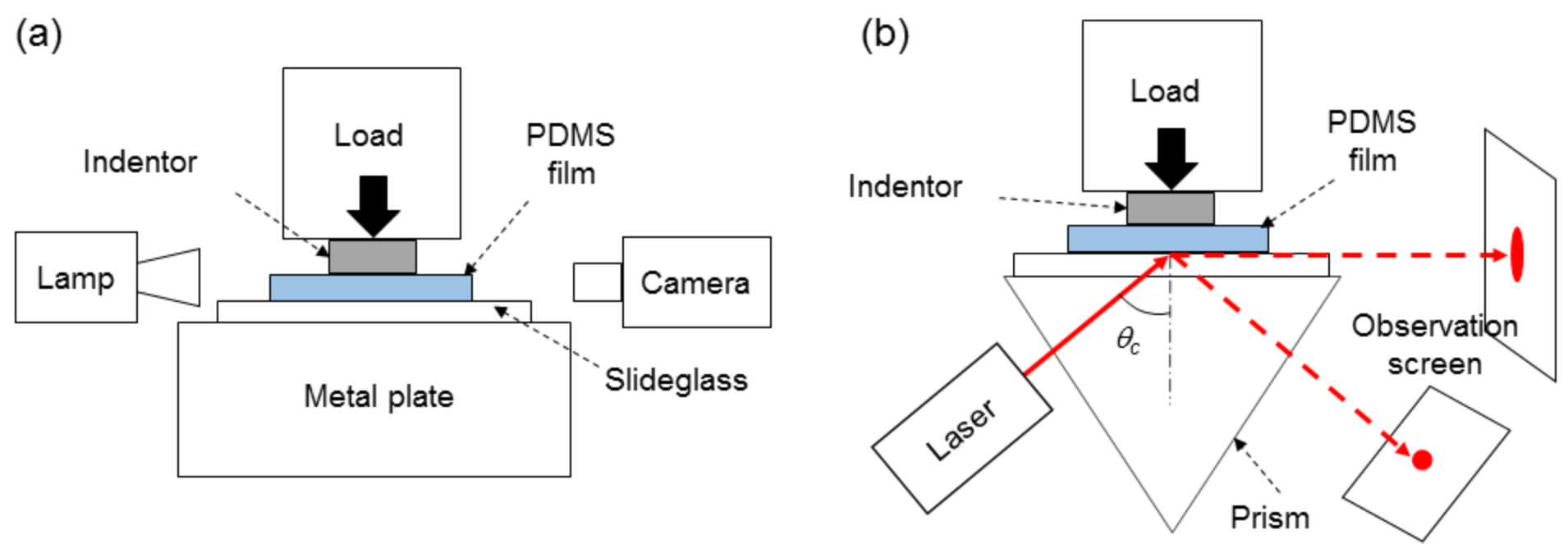
(a)
Load
Indentor
PDMS
film
Lamp
Camera
Slideglass
Metal plate
(b)
Load
Indentor
PDMS
film
Observation
screen
θ_c
Laser
Prism

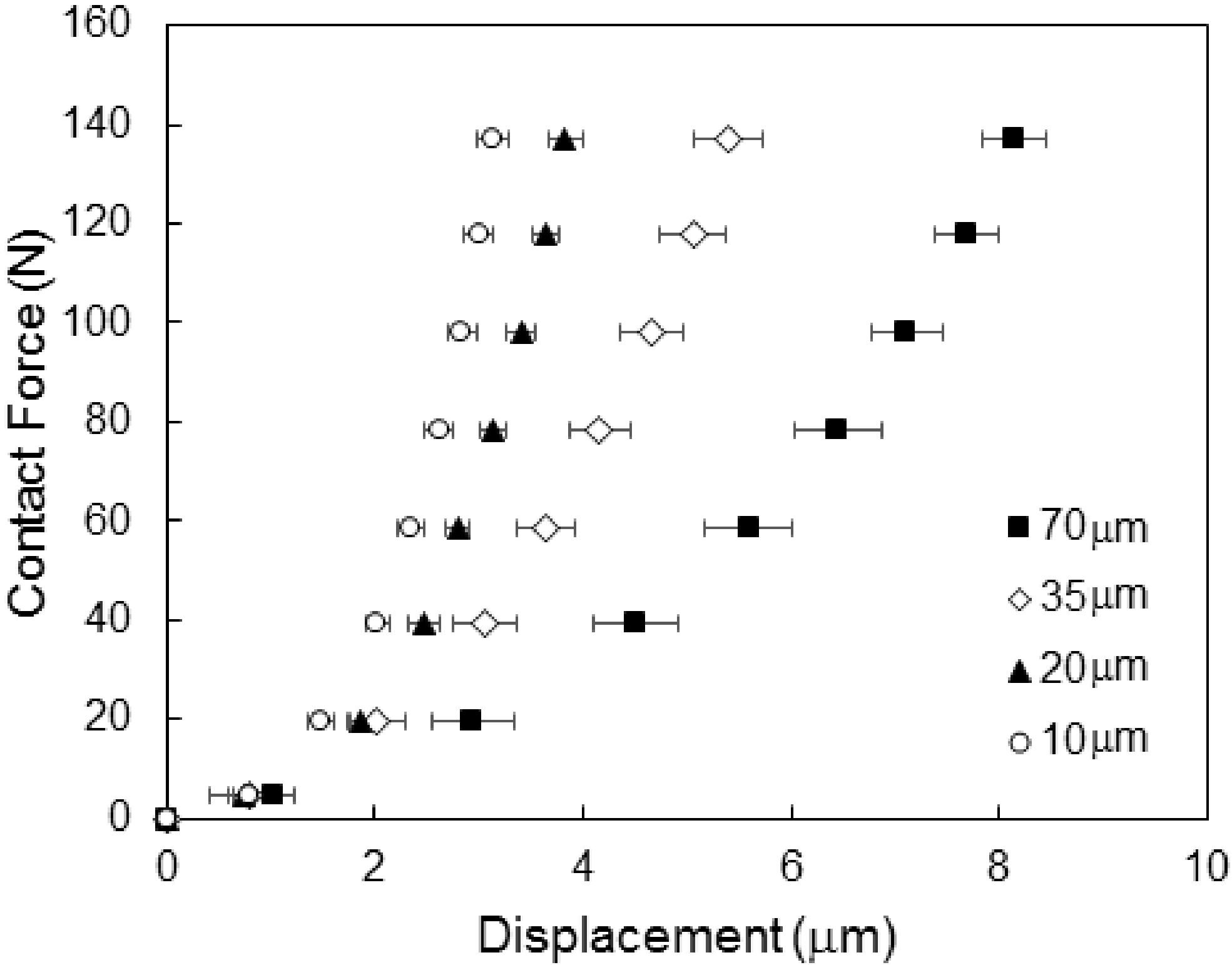
Contact Force (N)
160
140
120
100
80
60
40
20
0
0
2
4
6
8
10
Displacement (μm)
70 μm
35 μm
20 μm
10 μm

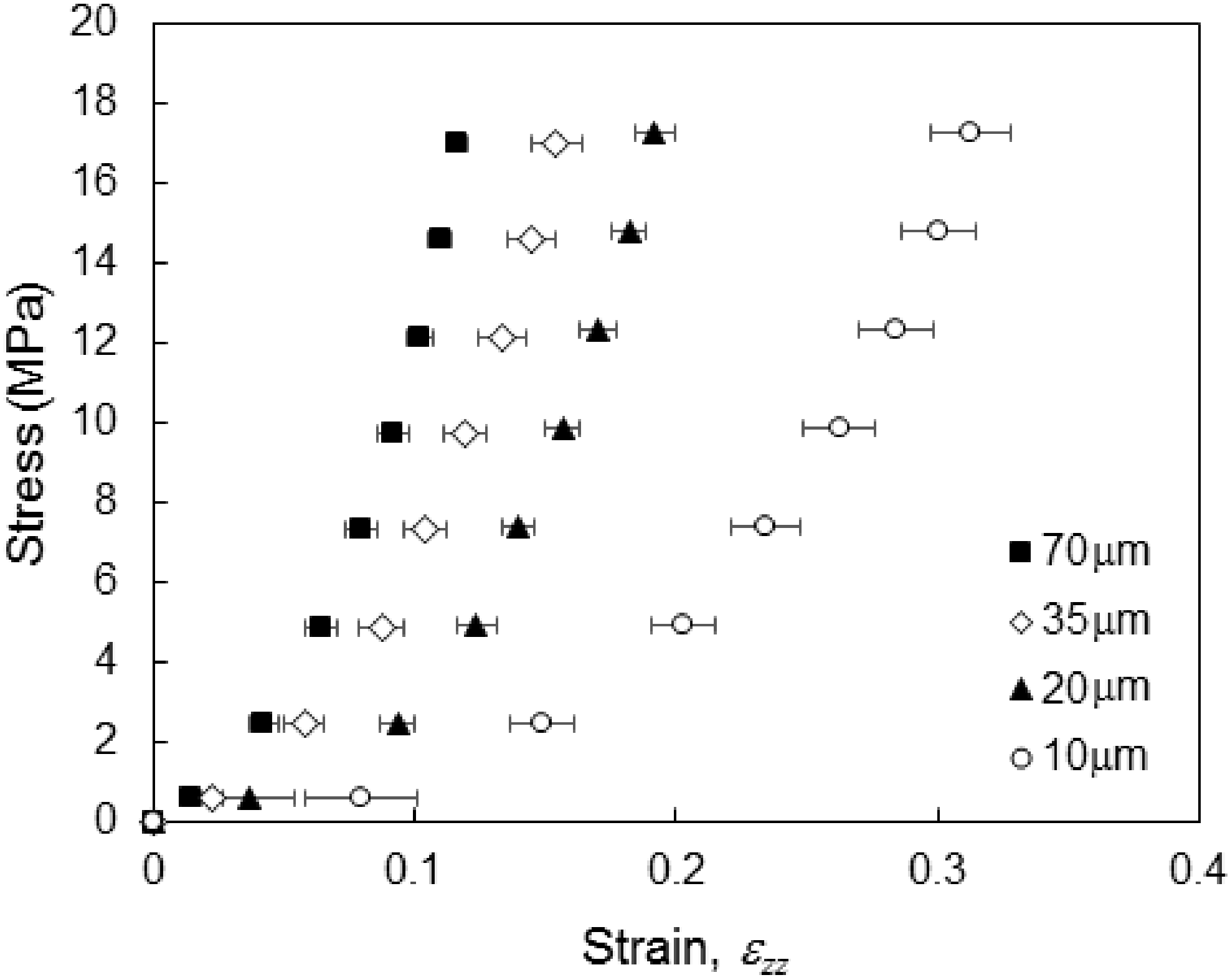
Stress (MPa)
Strain, ε_{zz}
0
2
4
6
8
10
12
14
16
18
20
0
0.1
0.2
0.3
0.4
70 µm
35 µm
20 µm
10 µm

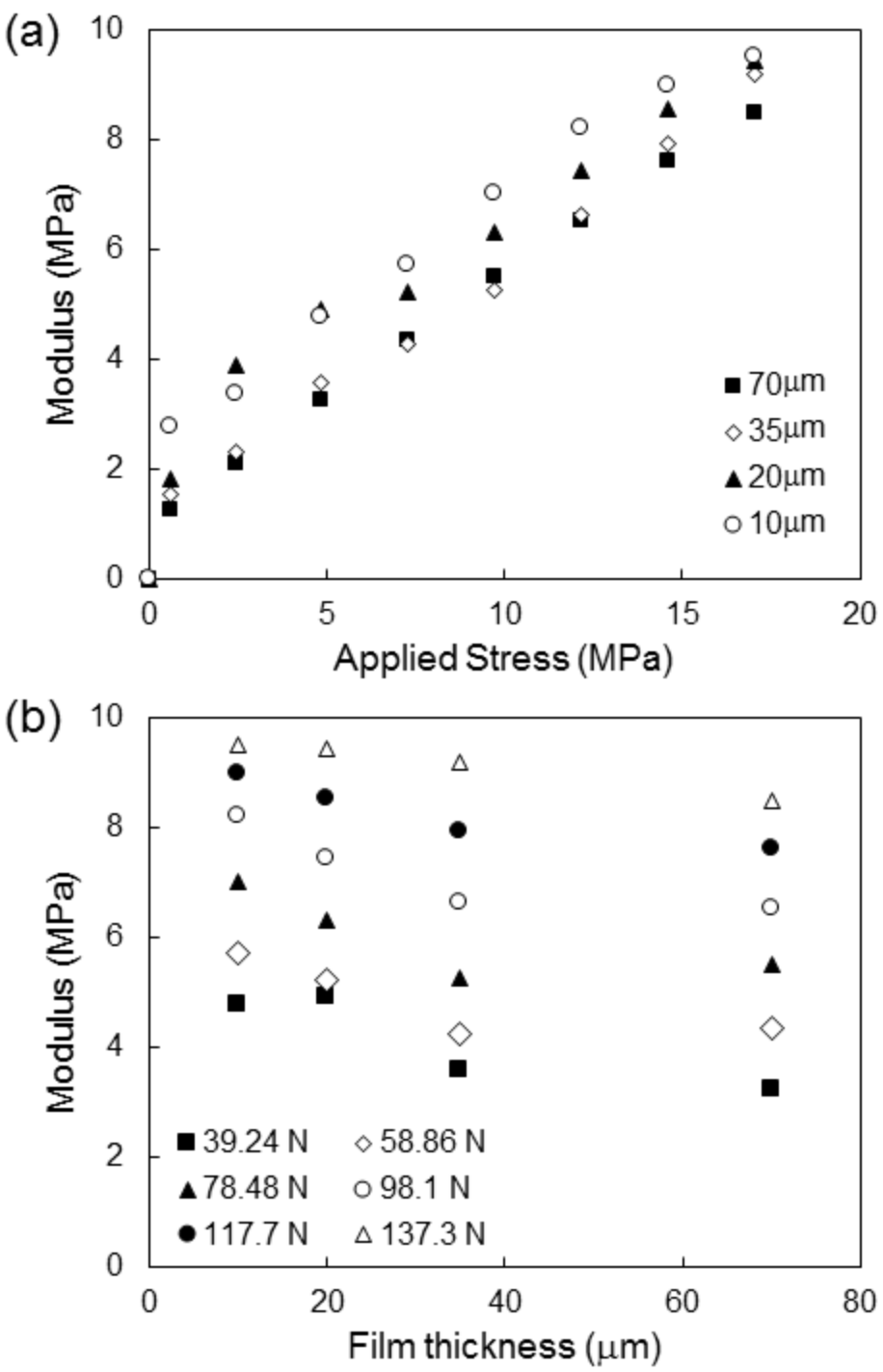
(a)
Modulus (MPa)
Applied Stress (MPa)
70μm
35μm
20μm
10μm
(b)
Modulus (MPa)
Film thickness (μm)
39.24 N
58.86 N
78.48 N
98.1 N
117.7 N
137.3 N

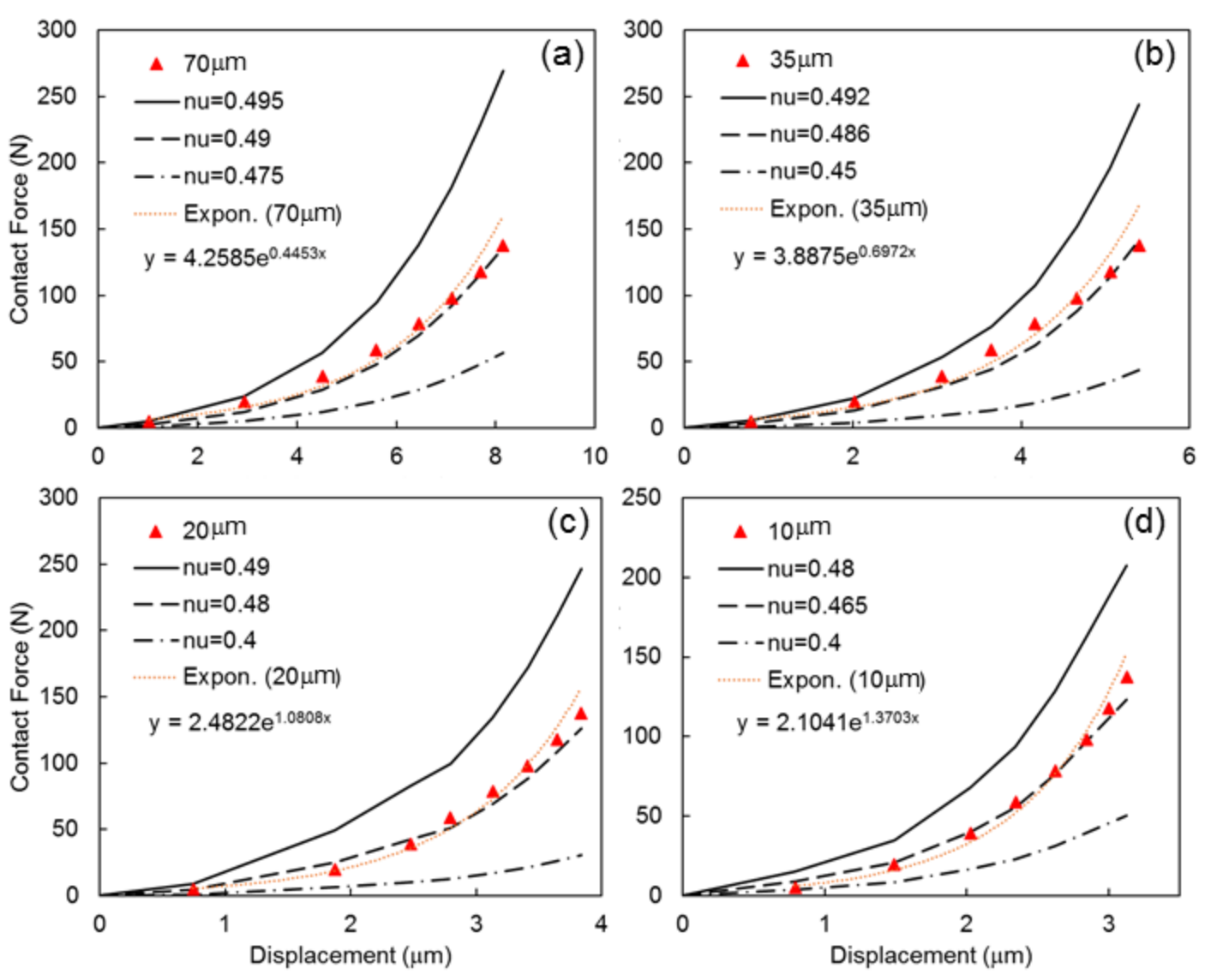
(a)
70μm
nu=0.495
nu=0.49
nu=0.475
Expon. (70μm)
y = 4.2585e^0.4453x
(b)
35μm
nu=0.492
nu=0.486
nu=0.45
Expon. (35μm)
y = 3.8875e^0.6972x
(c)
20μm
nu=0.49
nu=0.48
nu=0.4
Expon. (20μm)
y = 2.4822e^1.0808x
(d)
10μm
nu=0.48
nu=0.465
nu=0.4
Expon. (10μm)
y = 2.1041e^1.3703x
Contact Force (N)
Displacement (μm)

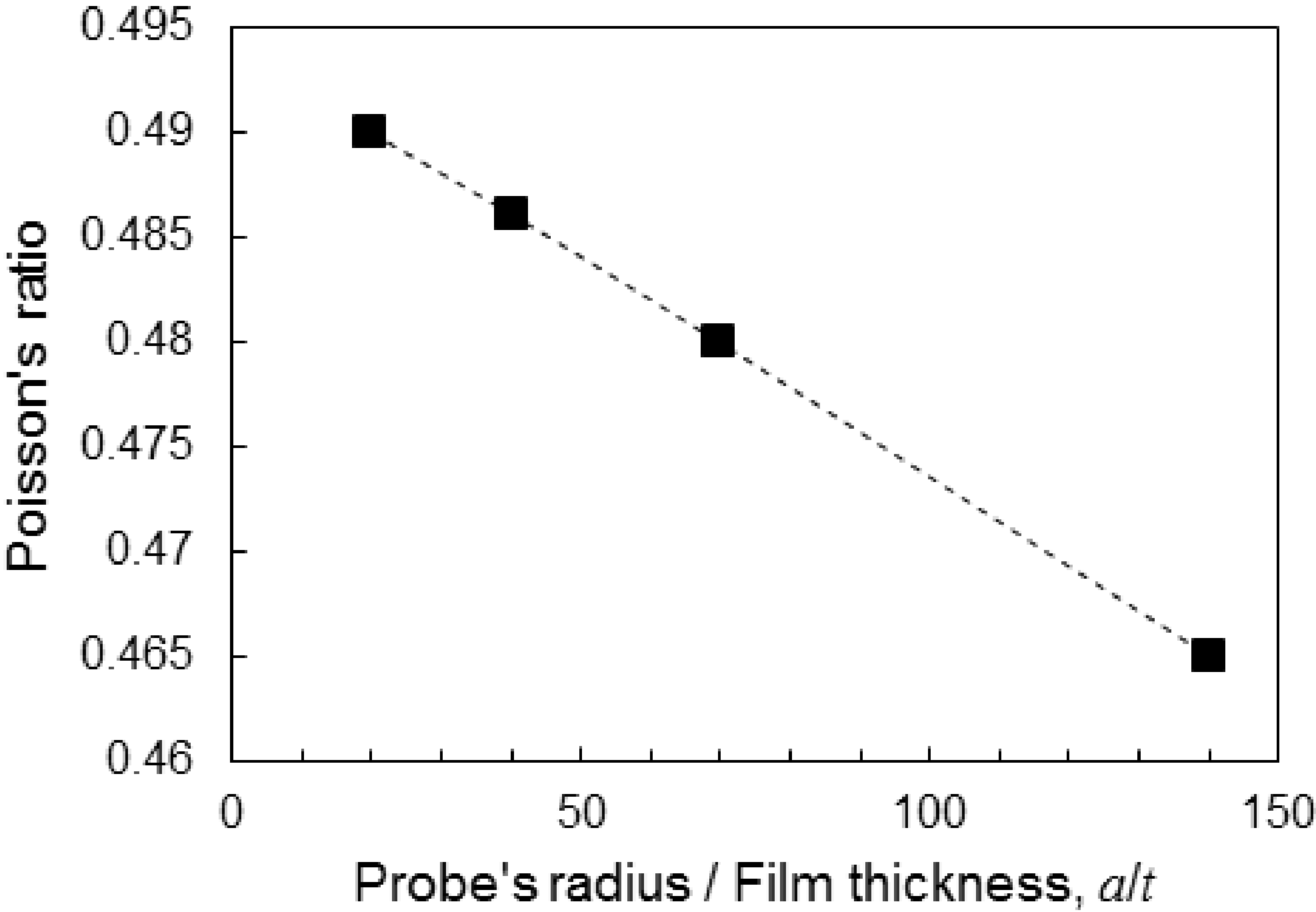
0.495
0.49
0.485
0.48
0.475
0.47
0.465
0.46
Poisson's ratio
0
50
100
150
Probe's radius / Film thickness, a/t

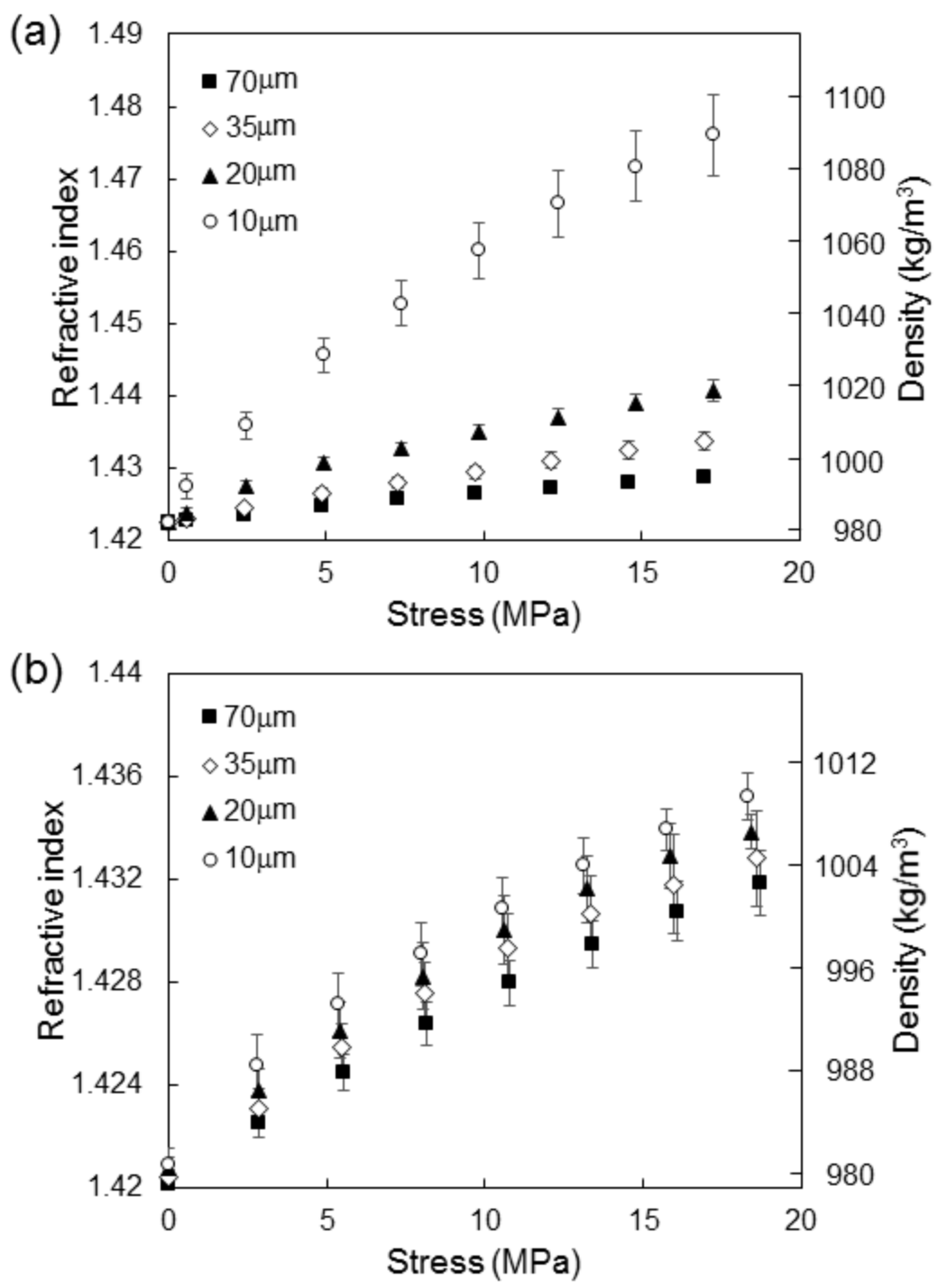
(a)
Refractive index
Density (kg/m3)
Stress (MPa)
70μm
35μm
20μm
10μm
1.49
1.48
1.47
1.46
1.45
1.44
1.43
1.42
1100
1080
1060
1040
1020
1000
980
0
5
10
15
20
(b)
Refractive index
Density (kg/m3)
Stress (MPa)
70μm
35μm
20μm
10μm
1.44
1.436
1.432
1.428
1.424
1.42
1012
1004
996
988
980
0
5
10
15
20

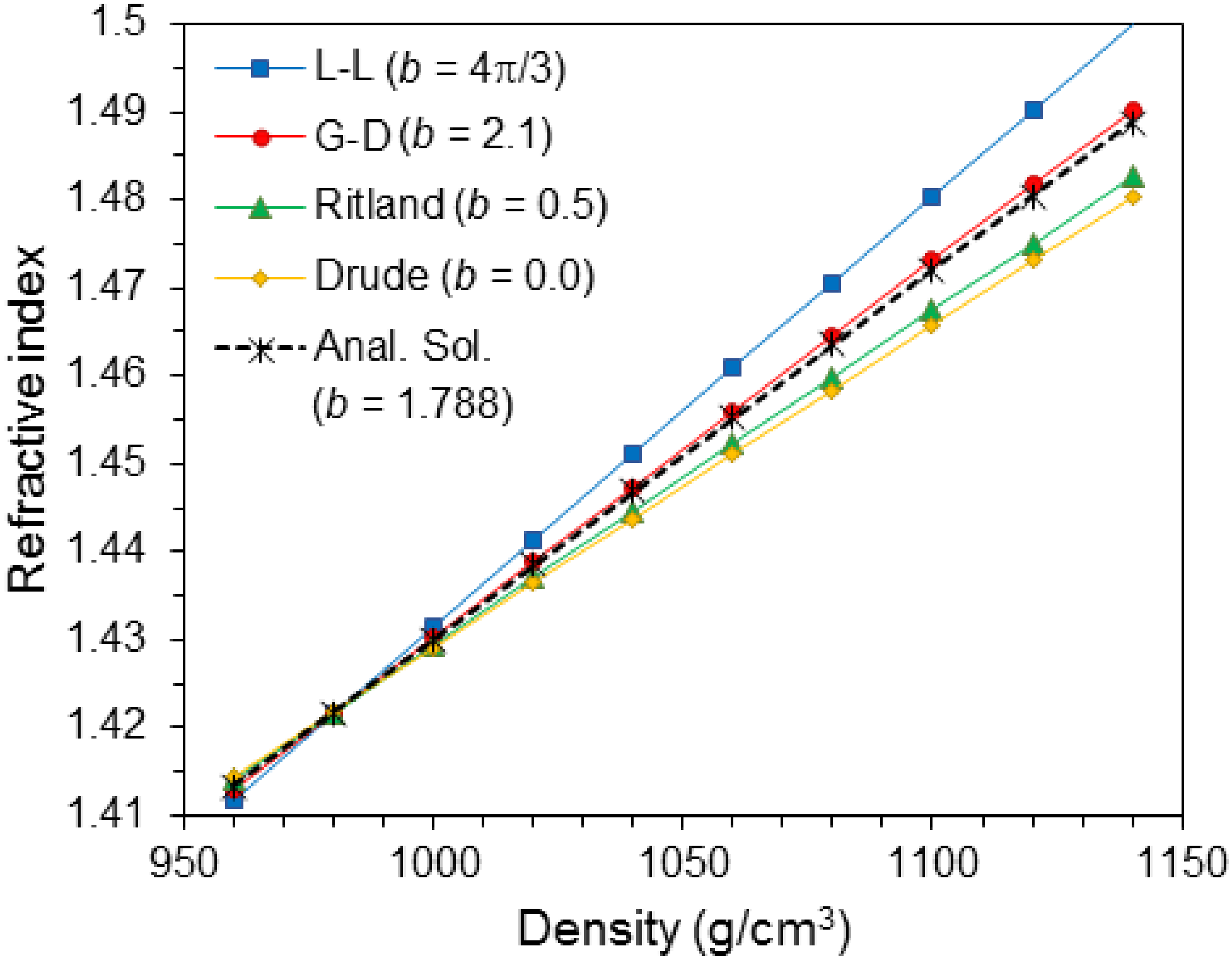
L-L ($b = 4\pi/3$)
G-D ($b = 2.1$)
Ritland ($b = 0.5$)
Drude ($b = 0.0$)
Anal. Sol.
($b = 1.788$)
Refractive index
1.5
1.49
1.48
1.47
1.46
1.45
1.44
1.43
1.42
1.41
950
1000
1050
1100
1150
Density (g/cm^3)

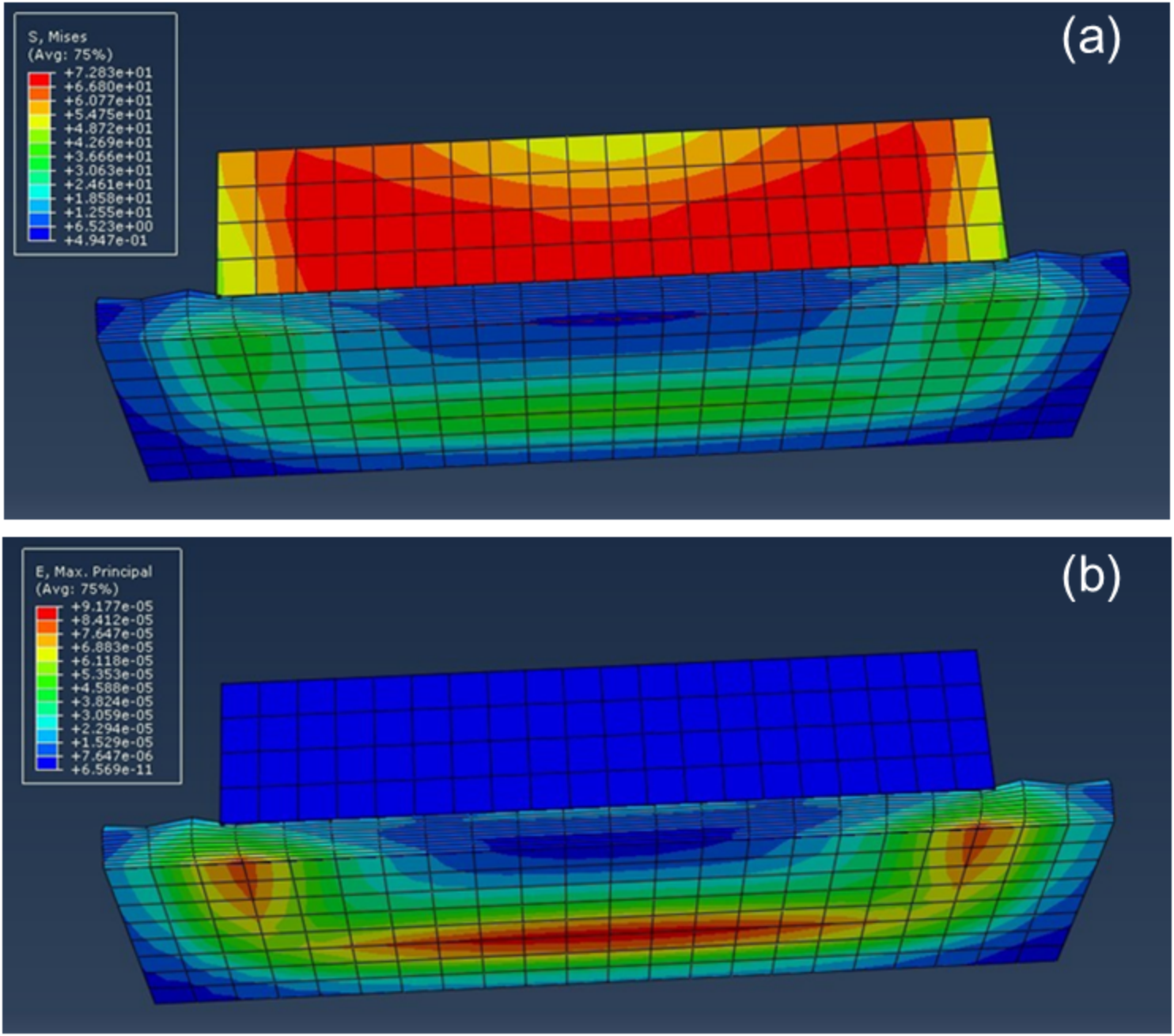
S, Mises
(Avg: 75%)
+7.283e+01
+6.680e+01
+6.077e+01
+5.475e+01
+4.872e+01
+4.269e+01
+3.666e+01
+3.063e+01
+2.461e+01
+1.858e+01
+1.255e+01
+6.523e+00
+4.947e-01
(a)
E, Max. Principal
(Avg: 75%)
+9.177e-05
+8.412e-05
+7.647e-05
+6.883e-05
+6.118e-05
+5.353e-05
+4.588e-05
+3.824e-05
+3.059e-05
+2.294e-05
+1.529e-05
+7.647e-06
+6.569e-11
(b)

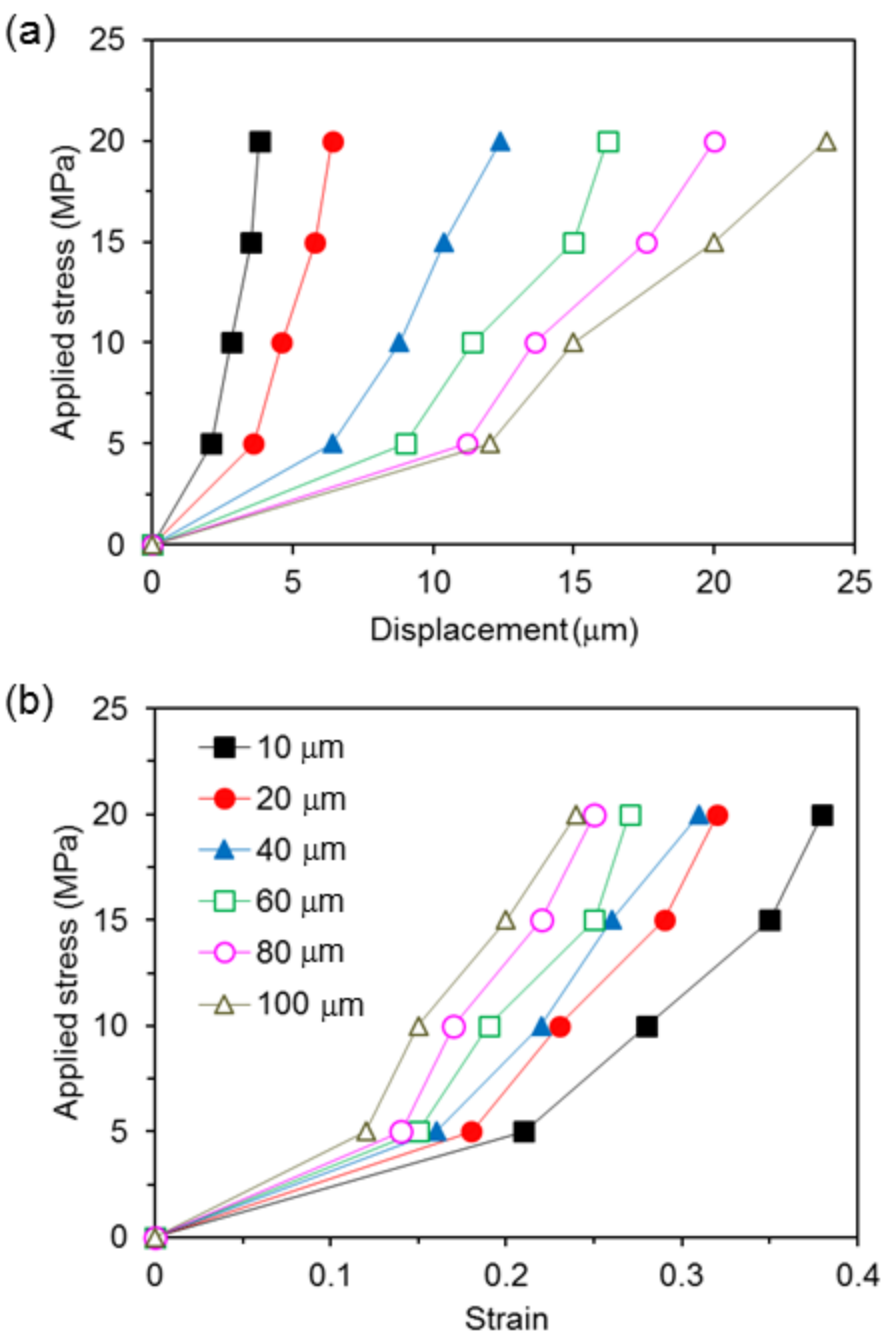
(a)
Applied stress (MPa)
Displacement (μm)
0
5
10
15
20
25
(b)
10 μm
20 μm
40 μm
60 μm
80 μm
100 μm
Applied stress (MPa)
Strain
0
0.1
0.2
0.3
0.4

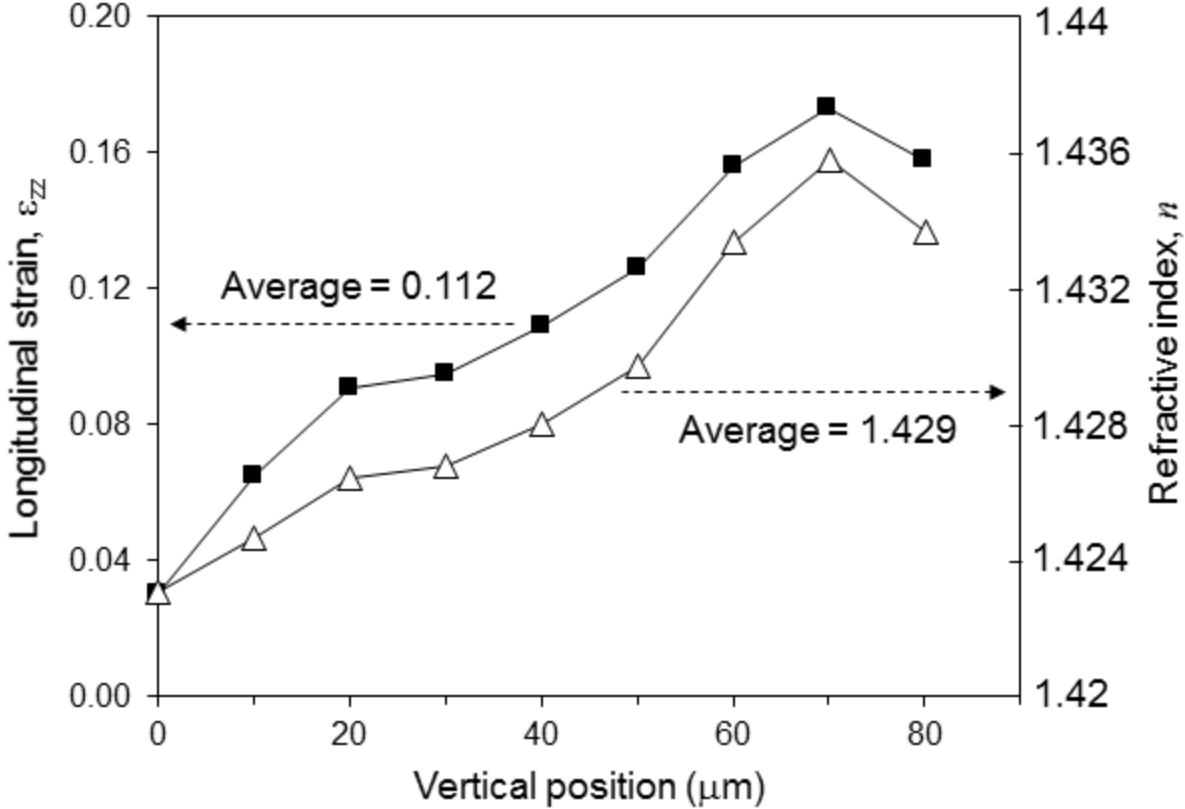
0.20
0.16
0.12
0.08
0.04
0.00
Longitudinal strain, ε_{zz}
1.44
1.436
1.432
1.428
1.424
1.42
Refractive index, n
Average = 0.112
Average = 1.429
0
20
40
60
80
Vertical position (μm)

Cross-section view of stress contour maps